

# Water-stable porous Al<sub>24</sub> Archimedean solids for removal of trace iodine

Received: 9 August 2022

Accepted: 20 October 2022

Published online: 04 November 2022

Check for updates

Ya-Jie Liu<sup>1,2</sup>, Yi-Fan Sun<sup>1</sup>, Si-Hao Shen<sup>1</sup>, San-Tai Wang<sup>1</sup>, Zhuang-Hua Liu<sup>1</sup>, Wei-Hui Fang<sup>1</sup> , Dominic S. Wright<sup>3</sup> & Jian Zhang<sup>1</sup>

In this paper, we report a unique type of core-shell crystalline material that combines an inorganic zeolitic cage structure with a macrocyclic host arrangement and that can remove trace levels of iodine from water effectively. These unique assemblies are made up of an inorganic Archimedean truncated hexahedron (*tcu*) polyhedron in the kernel which possesses six calixarene-like shell cavities. The cages have good adaptability to guests and can be assembled into a series of supramolecular structures in the crystalline state with different lattice pore shapes. Due to the unique core-shell porous structures, the compounds are not only stable in organic solvents but also in water. The characteristics of the cages enable rapid iodine capture from low concentration aqueous I<sub>2</sub>/KI solutions (down to 4 ppm concentration). We have studied the detailed process and mechanism of iodine capture and aggregation at the molecular level. The facile synthesis, considerable adsorption capacity, recyclability, and  $\beta$ - and  $\gamma$ -radiation resistance of the cages should make these materials suitable for the extraction of iodine from aqueous effluent streams (most obviously, radioactive iodide produced by atomic power generation).

Volatile radioactive species present in water cooling streams from nuclear fission reactors pose a serious threat to human health and the environment. Radioactive <sup>131</sup>I ( $t_{1/2}$  = 8.02 days) and <sup>129</sup>I ( $t_{1/2}$  = 15.7 million years) which are common decay products both pose a significant long-term health risk due to  $\beta$  and  $\gamma$  radioactive decay<sup>1–3</sup>. Therefore, there is an urgent need for materials that can capture iodine from aqueous effluents. Recent advances in this field together with synthetic chemistry have led to the development of materials capable of the removal of radioactive iodine. Currently, solid-phase adsorption includes ion exchange<sup>4</sup>, forming precipitates<sup>5</sup>, and chemical bonding<sup>6</sup>, which have notable advantages due to easy handling, avoidance of secondary pollution, and high removal efficiency<sup>7</sup>. Solid crystalline materials with long-range order are useful models for elucidation of the mechanism of radioactive element capture at the molecular level and may help in the design and synthesis of advanced materials<sup>8–10</sup>. Some crystalline materials, such as zeolites<sup>11,12</sup>, metal-organic frameworks (MOFs)<sup>13,14</sup>,

and hydrogen-bonded organic frameworks (H<sub>2</sub>O<sub>2</sub>)<sup>15</sup>, have been applied to water-phase iodide ion capture.

Supramolecular materials and cage compounds have also illustrated the potential for iodine removal as a result of their intramolecular and intermolecular host cavities for guest inclusion<sup>16–20</sup>. Considering ion exchange, cationic aluminum oxo clusters are more suitable candidates for capturing iodide ions than extensively studied polyoxometalate anions<sup>21,22</sup>. However, despite their wide application in water treatment (e.g., toxic arsenate adsorption), there are no studies of iodide anion removal from water reported. This may be due to their dense Keggin-type and Brucite-like cage<sup>23–25</sup> structures, the lack of suitable sites (such as conjugated groups) and appropriate cavities for absorption, and their poor crystallinity (i.e., limiting studies of the binding mechanisms from crystallographic analysis). As noted above, well-studied zeolites are stable with high adsorption and separation properties, while supramolecular cage materials have confined cavities

<sup>1</sup>State Key Laboratory of Structural Chemistry, Fujian Institute of Research on the Structure of Matter, Chinese Academy of Sciences, Fuzhou, Fujian 350002, P. R. China. <sup>2</sup>University of Chinese Academy of Sciences, Chinese Academy of Sciences, Beijing 100049, P. R. China. <sup>3</sup>The Yusuf Hamied Chemistry Department, Cambridge University, Lensfield Road, Cambridge CB2 1EW, UK. e-mail: [fwh@fjirsm.ac.cn](mailto:fwh@fjirsm.ac.cn); [zhj@fjirsm.ac.cn](mailto:zhj@fjirsm.ac.cn)

and abundant capture sites. If the characteristics of the two can be combined (microporous zeolite channels and supramolecular macrocyclic sites), it might be possible to form a unique type of porous material for the efficient removal of iodide ions in water.

Based on the above considerations and our previous work on aluminum molecular rings<sup>26–29</sup>, we herein report the aggregation of the aluminum molecular rings into cationic core–shell  $\text{Al}_{24}$  Archimedean solids and their performance in removing iodide from water. The  $\text{Al}_{24}$  Archimedean solids consist of a pure-inorganic truncated hexahedron (**tcu**) cage in the core together with six calixarene-like macrocyclic cavities. Notably, this assembly is an unprecedented combination of an inorganic zeolite-like cage with macrocyclic units. The macrocyclic cavities are situated on six faces of the **tcu** polyhedron, consequently, we refer to this unique class of compounds as “aluminum macrocycle-faced cages” (abbreviated as **AIMCs**). The **AIMCs** are well adapted to the guests, exhibiting key features required for iodide extraction—self-assembly, recrystallizability, and reversible ion exchange (Fig. 1). They exhibit high chemical stability, including excellent water stability, and can be prepared in large quantities. The  $\text{Al}_{24}$  cation units present not only exhibit a fast adsorption response but also a low capture concentration for iodine ions, indicating their potential as iodide adsorbents in water. The iodide capture and aggregation processes have been revealed at the molecular level using crystal-to-crystal diffraction studies.

## Results

### Archimedean $\text{Al}_{24}$ cage structure

All of the **AIMC** host–guest complexes have similar molecular units in which the host is the cation  $[\text{Al}_{24}(\text{BA})_{12}(\text{EtO})_{24}(\text{OH})_{32}]^{4+}$  ( $\text{Al}_{24}$ ) (BA = benzoate), constructed from truncated hexahedron (**tcu**) made up of six octagonal  $\text{Al}_8$  faces and eight triangular  $\text{Al}_3$  faces (Fig. 2a, Supplementary Movie 1). Of all the 13 Archimedean polyhedra the **tcu** is the only one composed of triangles and octagons (Supplementary Figs. 1–4). In previous rarely reported **tcu** cages, organic ligands are used as edges, such as in  $[\text{V}_{24}\text{O}_{24}(\text{C}_4\text{O}_4)_{12}(\text{OCH}_3)_{32}]^{8-}$  reported by Hartl et al.<sup>30</sup>, and the  $\text{Ag}_{24}\text{L}_{16}$  cage reported by Fujita et al.<sup>31</sup>. Notably,  $\text{Al}_{24}$  is a rare example possessing a purely inorganic **tcu** cage. There are four hydroxyl groups that point towards the center of each octagonal face of the  $\text{Al}_{24}$  unit (Supplementary Fig. 5), and one hydroxyl group on every triangular face (Supplementary Fig. 6), forming an internal inorganic cubic cavity (the available volume being  $\sim 320 \text{ \AA}^3$ ) (Supplementary Fig. 7). The  $\text{Al}_{24}$  core is capped by six calixarene-like macrocyclic fragments over each of the octagonal faces of the **tcu** core. These macrocyclic units are composed of 8  $\text{Al}^{3+}$  cations which are bonded together using a combination of  $\mu_2\text{-OH}$ , benzoate, and

ethoxide groups. The dimensions of the macrocyclic apertures are very similar to that found in calix[4]arene (the height, lower diameter, and upper diameter are, respectively,  $4.83 \times 4.97 \times 19.18 \text{ \AA}^3$  vs.  $4.51 \times 4.48 \times 16.16 \text{ \AA}^3$  for calix[4]arene) (Supplementary Fig. 8). Hence, the whole  $\text{Al}_{24}$  arrangement has a molecular diameter of  $\sim 2.0 \text{ nm}$  (Supplementary Figs. 9–11). Compared with traditional metal-organic cages with a single cavity<sup>32–34</sup>, the  $\text{Al}_{24}$  cage, therefore, has a ‘two-tier’ cavity arrangement, which combines the characteristics of an inorganic metal cage with that of a calixarene, and possesses inorganic hydrophilic and organic hydrophobic cavities (Supplementary Movie 2).

As shown in Fig. 2b, the molecular polyhedron possesses a highly symmetrical geometry and a five-level nested structure (Supplementary Fig. 12), i.e., from the inner inorganic component to the outer organic components,  $\text{O}_8$  **cube** @ **tro** @ **tcu** @ **rco** @ **cuo**. For the inner inorganic fragment, eight  $\mu_3\text{-OH}$  groups form a centered  $\text{O}_8$  **cube** (with a diameter of  $4.47 \text{ \AA}$ ). The second  $\text{O}_{24}$  shell is a truncated octahedral (**tro**) shell made up of 24  $\mu_2\text{-OH}$  groups (with a diameter of  $8.16 \text{ \AA}$ ). As far as the organic ligands are concerned, 24 ethoxide groups are situated on the edges of triangular faces constituting an  $(\text{OR})_{24}$  rhombicuboctahedron (**rco**) subunit (with a diameter of  $9.25 \text{ \AA}$ ), while the benzoate ligands bridge adjacent  $\text{Al}_3(\mu_3\text{-OH})$  segments and assemble into a  $(\text{BA})_{12}$  cuboctahedron (**cuo**) arrangement (with a diameter of  $19.18 \text{ \AA}$ ).

The peripheral macrocyclic units of the  $\text{Al}_{24}$  host can trap a large array of guests of different sizes, shapes, and charges, including neutral water molecules, ethanol, n-propyl alcohol, nitrate, and halide anions (Fig. 3a, Supplementary Figs. 13–19). These guest molecules form H-bonding interactions with the four OH groups of the macrocyclic units with  $\text{O}\cdots\text{H}\cdots\text{O}$  range  $2.823\text{--}3.354 \text{ \AA}$  and  $\text{O}\cdots\text{H}\cdots\text{X}$  ( $\text{X} = \text{Cl}, \text{Br}, \text{I}$ ) range  $3.131\text{--}3.728 \text{ \AA}$  (Supplementary Figs. 20–25), which are close to those reported in the literature<sup>35–38</sup>. The six guests that are accommodated form an octahedron (sizes:  $11.19 \text{ \AA} \times 7.92 \text{ \AA}$ – $13.76 \text{ \AA} \times 9.73 \text{ \AA}$ , Supplementary Fig. 13). The depth and aperture size of these  $\text{Al}_8$  macrocyclic subunits vary depending on the guest present (depth:  $4.58\text{--}5.49 \text{ \AA}$ , aperture:  $16.42\text{--}18.76 \text{ \AA}$ ) (Supplementary Table 1).

The interaction of the  $\text{Al}_{24}$  cations with these guests generates a diverse range of supramolecular lattice arrangements, including monoclinic **AIMC-1** (space group,  $C2/c$ ) and **AIMC-3** (space group,  $P2_1/n$ ), triclinic **AIMC-2** and **AIMC-4** (space group,  $P-1$ ), trigonal **AIMC-7** (space group,  $R-3$ ), and cubic **AIMC-5** (space group,  $Ia-3$ ), as well as **AIMC-6** (space group,  $Ih-3m$ ) (Fig. 3b). Their supramolecular packing in the solid state correlates with the crystal morphology (Supplementary Fig. 26). Typically, the solid-state packing involves the back-to-back alignment of two  $\text{Al}_8$  macrocyclic subunits on adjacent  $\text{Al}_{24}$

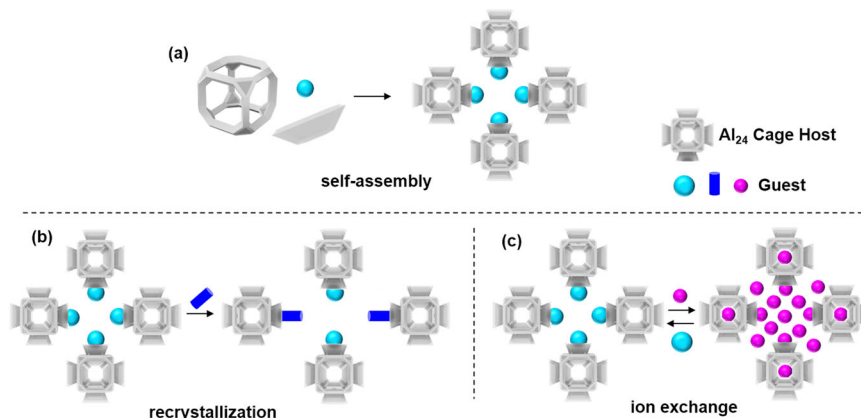


**Fig. 1 | The supramolecular assembly of the  $\text{Al}_{24}$  cages.** **a** One-step **AIMC** self-assembly results in the integration of an inorganic **tcu** cage containing calixarene-like macrocyclic units. **b** Recrystallization of the **AIMC** results in a lattice with

embedded guest molecules. **c** Reversible single crystal-to-single crystal ion exchange process of the **AIMC**.

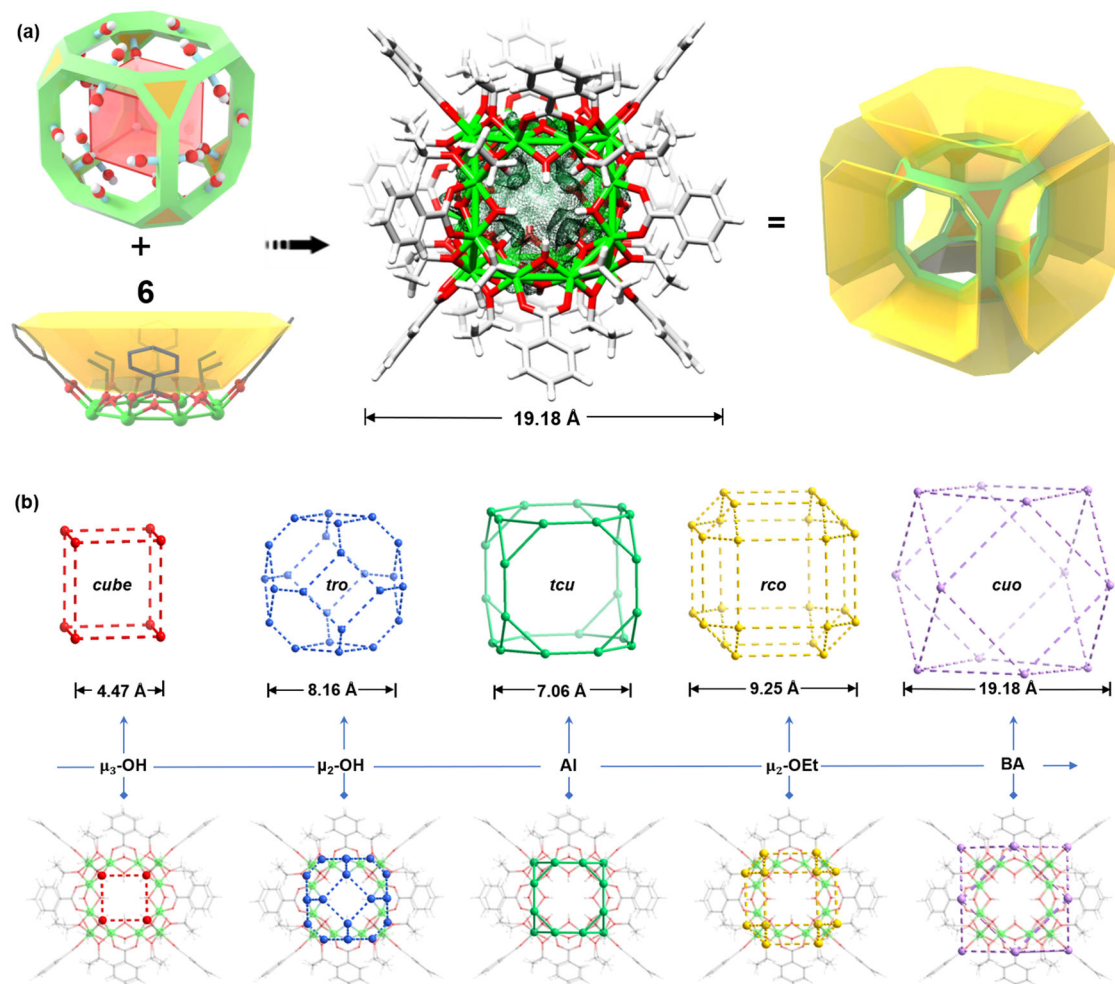


**Fig. 2 | The molecular structure of the  $Al_{24}$  Archimedean cage. a** Illustration of the assembly and structural model of the inner inorganic *tcu* core and calixarene-like organic subunits (atom color code: Al: bright green; O: red; C: gray; H: white). The size of the *tcu* cage is ca. 1.9 nm based on the distance between the BA ligands. **b** Quintuple structural symmetric anatomy of the  $Al_{24}$  Archimedean solid. The inner

shell is an  $O_8$  cube, the second shell is an  $O_{24}$  truncated octahedron (*tro*) cage, the third shell is an  $Al_{24}$  truncated hexahedron (*tcu*) cage, the fourth shell is an  $(OR)_{24}$  rhombicuboctahedron (*rcu*) cage, and the outermost shell is a  $(BA)_{12}$  cuboctahedron (*cuo*) cage.

cages which accommodate a pair of guests (Supplementary Figs. 27–32). The shape and size of this coordination pocket and the alignment of the macrocyclic units are highly dependent on the guests (Supplementary Figs. 33–38), being spindle- (Supplementary Fig. 33a), peanut- (Supplementary Fig. 33b), or Z-shaped (Supplementary Fig. 33c), and with a distance between the two macrocyclic units varying in the order  $H_2O$  cavity (4.794 Å) <  $Cl^-$  cavity (7.625 Å) < ethanol cavity (7.625–7.706 Å) < n-propanol cavity (7.892 Å) <  $Br^-$  cavity (9.156 Å) <  $NO_3^-$  cavity (10.483–10.883 Å) (Supplementary Figs. 27–32). The presence of small anions as guests ( $Cl^-$ ,  $Br^-$  and  $I^-$ ) not only influences the solid-state packing of the cages but these anions are also present within the center of the cage (H-bonded within the eight OH groups of the central cubic  $O_8$  unit). **AIMC-1** to **AIMC-5** contain disordered  $NO_3^-$  anions within their  $O_8$  cavities, with the number decreasing from 2 (in **AIMC-1** to **AIMC-3**) to 1 (in **AIMC-4** and **AIMC-5**) in the presence of halide ions (Supplementary Figs. 39–42). In **AIMC-6** containing no  $NO_3^-$ , this site is occupied by an  $I^-$  anion (Supplementary Fig. 42c). **AIMC-7** contains a cationic macrocycle in its supramolecular arrangement  $[(Al_6(BA)_6(OEt)_6(NO_3)_2)_{0.5}]^{2+}$  which links units of  $Al_{24}$  together (Supplementary Figs. 43–49). The  $Al_6$ -ring unit of the latter contains 6  $Al^{3+}$  centers held together by 6 benzoate ligands, 6 alkoxides, and two  $NO_3^-$  anions. To the best of our knowledge, such a cationic  $\{Al_6\}$  ring has not been reported previously, although similar

neutral  $Al$ -macrocycles have been observed by us<sup>26,28</sup>. The  $Al_{24}$  cations are surrounded by six  $Al_6$ -rings in **AIMC-7** (Supplementary Figs. 13 and 46), thus, there are dual-Platonic octahedra present, one is formed by the six capping ethanol guests, and the other is created via six  $Al_6$  rings (Supplementary Fig. 46). The isolation of **AIMC-7**, containing these  $Al_6$  macrocyclic cations, provides some potential insight into the mechanism of formation of the  $Al_{24}$  cation itself, which potentially results from the condensation of these smaller rings during the reaction.

Supramolecular assembly can also be achieved by recrystallization from acetonitrile. An interesting stack transformation occurs on crystallization of **AIMC-5** from *1a-3* (cube crystals) to  $P2_1/n$  in **AIMC-8** (parallelogram crystals) from acetonitrile (Fig. 3, Supplementary Figs. 50–53), with the guests experiencing a slight adjustment in coordination environment. The phase purity for **AIMC-1** to **AIMC-8** was validated by their powder X-ray diffraction (PXRD) patterns (Supplementary Figs. 54–61). The presence of some of the anion guests can be confirmed by energy-dispersive X-ray dispersive spectroscopies (EDS) (Supplementary Figs. 62–69) and Fourier transform infrared (FT-IR) spectroscopies (Supplementary Figs. 70–77). The apparent band gaps for colorless compounds (except **AIMC-6**) are in the range of 4.2–4.3 eV (Supplementary Figs. 78–85). Furthermore, thermogravimetric analysis (TGA) of **AIMC-1** to **AIMC-7** showed that these cages

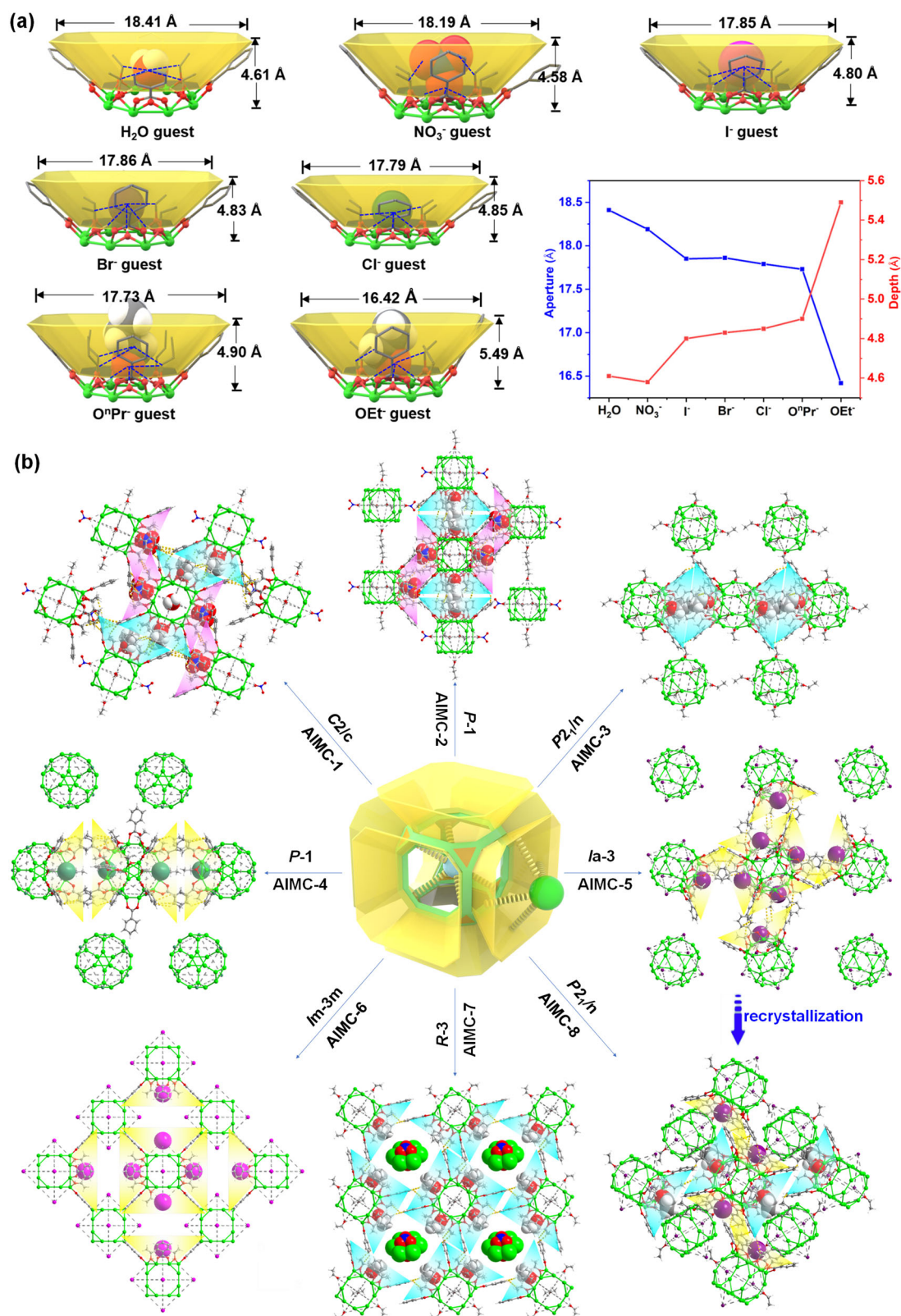


**Fig. 3 | Supramolecular lattice assemblies between the cationic  $\text{Al}_{24}$  host and a variety of guests.** **a** The  $\text{Al}_{24}$  macrocyclic subunits adapt to the accommodated  $\text{H}_2\text{O}$  (in AIMC-1),  $\text{NO}_3^-$  (in AIMC-1),  $\text{I}^-$  (in AIMC-6),  $\text{Br}^-$  (in AIMC-5),  $\text{Cl}^-$  (in AIMC-4),  $\text{O}^i\text{Pr}$  (in AIMC-2) and  $\text{OEt}^-$  (in AIMC-3) guests. The blue dotted lines indicate that there are strong hydrogen bond interactions between two atoms (the details of the hydrogen bond interactions are provided in Supplementary Figs. 20–25). **b** Packing diagrams of AIMC-1–AIMC-8. Hydrogen-bond interactions between neighboring

$\text{Al}_{24}$  units are shown with yellow dotted lines. ( $\text{NO}_3^-$  macrocyclic cavities: pink; alcohol/alkoxide macrocyclic cavities: blue; halogen ion macrocyclic cavities: yellow). The molecular formulae of AIMC-1–AIMC-8 are, respectively:  $\text{Al}_{24}\cdot 4\text{NO}_3\cdot 2\text{HOEt}\cdot 2\text{H}_2\text{O}$  (AIMC-1),  $\text{Al}_{24}\cdot 4\text{NO}_3\cdot 4\text{HO}^i\text{Pr}$  (AIMC-2),  $\text{Al}_{24}\cdot 2\text{NO}_3\cdot 4\text{HOEt}\cdot 2\text{OEt}^-$  (AIMC-3),  $\text{Al}_{24}\cdot \text{NO}_3\cdot 3\text{Cl}^-$  (AIMC-4),  $\text{Al}_{24}\cdot \text{NO}_3\cdot 3\text{Br}^-$  (AIMC-5),  $\text{Al}_{24}\cdot 4\text{I}^-$  (AIMC-6),  $\text{Al}_{24}\cdot \text{H}\cdot \text{NO}_3\cdot 6\text{OEt}^-\cdot (\text{Al}_6(\text{BA})_6(\text{OEt})_6(\text{NO}_3)_2)_{0.5}$  (AIMC-7),  $\text{Al}_{24}\cdot \text{NO}_3\cdot 2\text{Br}^-\cdot \text{OEt}^-$  (AIMC-8) (Al: bright green; O: red; C: gray; H: white; N: blue; Cl: sea green; Br: purple; I: pink).

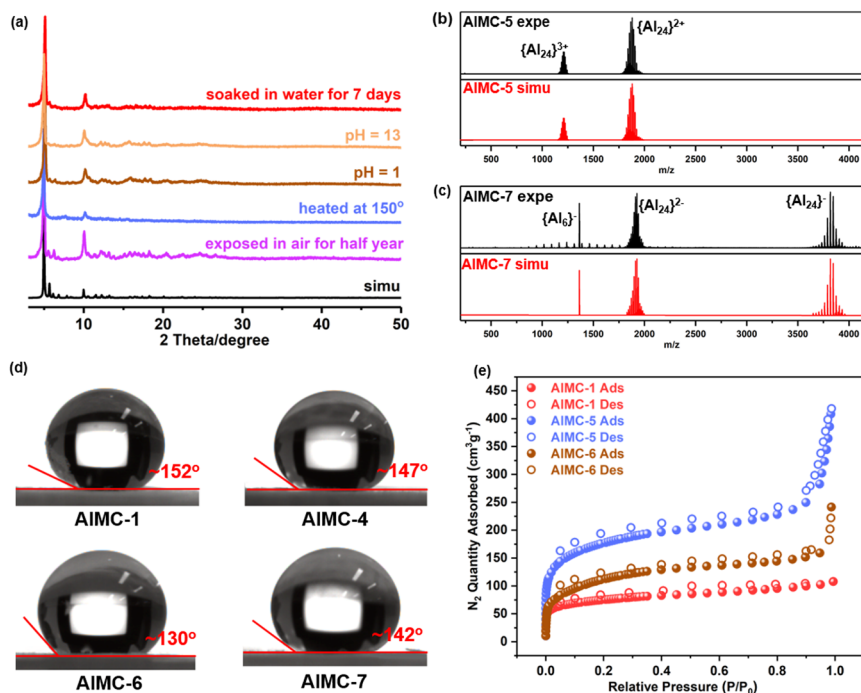


**Fig. 4 | Stability, wettability, and porosity measurements on selected cages.** **a** Structural stability of **AIMC-1** under different conditions. **b** Solution stability of **AIMC-5**: experimental and simulated mass spectra in MeCN under positive mode. **c** Solution stability of **AIMC-7**: experimental and simulated mass spectra in a mixed

solvent of MeCN and DMF (volume ratio: 20:1) under negative mode. **d** The wettabilities of **AIMC-1**, **AIMC-4**, **AIMC-6**, and **AIMC-7**. **e** The N<sub>2</sub> gas sorption isotherms at 77 K for **AIMC-1**, **AIMC-5**, and **AIMC-6**. Source data are provided as a Source Data file.

remain stable up to 170–180 °C under N<sub>2</sub> atmosphere (Supplementary Figs. 86–92).

### Stability characteristics

Stability is a critical issue that needs to be considered in systems with real-world applications. All of the compounds exhibit high air stability (e.g., **AIMC-1** is stable for more than half a year, Fig. 4a), thermal stability (e.g., **AIMC-1** remains crystalline at 150 °C, Fig. 4a and Supplementary Fig. 93), and a high degree of chemical stability. They are stable in common low-polarity organic solvents (Supplementary Figs. 94–100), and soluble in highly polar aprotic solvents, like acetonitrile (CH<sub>3</sub>CN), dimethylformamide (DMF) and dimethylsulfoxide (DMSO) (Supplementary Table 2). The stability of the cationic Al<sub>24</sub> unit was monitored by ESI-MS spectra (Fig. 4b, c and Supplementary Figs. 101–104, Supplementary Tables 3–8) and <sup>1</sup>H NMR spectroscopic analysis (Supplementary Fig. 105) by dissolving single crystals in acetonitrile or DMSO<sup>39</sup>. For example, ESI-MS analysis of **AIMC-5** gave a spectrum with two sets of dominant peaks assigned to [Al<sub>24</sub>(BA)<sub>12</sub>(μ<sub>3</sub>-OH)<sub>8</sub>(μ<sub>2</sub>-OH)<sub>x</sub>(OEt)<sub>48-x</sub>NO<sub>3</sub>]<sup>3+</sup> (x = 25–36) and [Al<sub>24</sub>(BA)<sub>12</sub>(μ<sub>3</sub>-OH)<sub>8</sub>(μ<sub>2</sub>-OH)<sub>x</sub>(OEt)<sub>48-x</sub>9CH<sub>3</sub>CN·NO<sub>3</sub>·Br]<sup>2+</sup> (x = 36–48) due to the loss of ethanol (Fig. 4b)<sup>40</sup>. The other major consecutive peaks in **AIMC-5** and their formulae are provided in Supplementary Table 7. In addition, the presence of the [Al<sub>6</sub>(BA)<sub>6</sub>(NO<sub>3</sub>)<sub>2</sub>(OH)<sub>11</sub>·(CH<sub>3</sub>CN)<sub>4</sub>]<sup>-</sup> ion observed in the negative-ion ESI-MS of **AIMC-7** strongly supported the crystallographic results (exp: 1363.10; cal: 1363.17) (Fig. 4c and Supplementary Table 8).

Water stability is an important property with respect to aqueous-phase iodide capture (see later in this paper). Water stability was evaluated by immersing as-prepared crystals of **AIMC-1** in water at different pH values for 24 h and was confirmed by the unchanged PXRD pattern (Fig. 4a). In order to evaluate the long-term stability, crystals of **AIMC-1** were soaked in water for 7 days at room temperature. Combined PXRD (Fig. 4a), Fourier transform infrared spectroscopy (FTIR) (Supplementary Fig. 106), and the preservation of the morphology of the transparent crystals (Supplementary Fig. 107)

indicated its good water stability. In addition, the nearly identical cell parameters encourage us to collect the single-crystal X-ray diffraction data on these water-exposed crystals (Supplementary Fig. 108). We find that in the product (**AIMC-1a**) the complete Al<sub>24</sub> *t*c<sub>u</sub> skeleton is preserved (Supplementary Fig. 109). The water stability of **AIMC-1** is presumably partly related not only to the presence of hydrophobic ligands which shield the internal Al<sup>3+</sup> ions from attack by H<sub>2</sub>O (Fig. 4d and Supplementary Fig. 110) but also to the presence of robust aluminum–oxygen bonds. Theoretical and experimental studies have proved that the presence of high valent metals, high nuclearity, and the presence of metal–oxygen bonds in metal clusters are key factors influencing water stability<sup>41–44</sup>.

The lattice void volumes for **AIMC-1** to **AIMC-7** are in a range of 16.9–49.0% using PLATON calculations. The N<sub>2</sub> sorption isotherms at 77 K were also obtained for **AIMC-1** to **AIMC-7**, and the calculated Brunauer–Emmett–Teller (BET)-specific surface areas are, respectively, 233.36, 132.87, 217.17, 182.39, 557.91, 370.47 and 161.04 m<sup>2</sup> g<sup>-1</sup> (Fig. 4e and Supplementary Fig. 111). The typical type-I isotherms for them indicate the existence of micropores in the crystals (Supplementary Fig. 112), suggesting they can be employed as potential adsorbents. In addition, they remain stable after the adsorption tests (Supplementary Fig. 113).

### Iodine adsorption

**AIMC-1** was chosen as the ideal candidate for adsorption experiments since it can be prepared on a large scale (Supplementary Figs. 114 and 115) and forms well-defined rectangular crystals (Fig. 5a) of uniform size (~50 μm, passed through a 200-mesh sieve, 20 mg). An aqueous solution of I<sub>2</sub>/KI was chosen as the reaction medium because it can function as an effective source of I<sup>-</sup>, I<sub>2</sub> and I<sub>3</sub><sup>-</sup> based on the dynamic equilibrium I<sub>2</sub> + I<sup>-</sup> ⇌ I<sub>3</sub><sup>-</sup><sup>13,45</sup>. Colorless crystals of **AIMC-1** undergo a noticeable color change within 1 minute by eye when immersed in this solution (Fig. 5b, c, Supplementary Movie 3), turning black after 30 min. Single-crystal X-ray diffraction proves that the NO<sub>3</sub><sup>-</sup> and EtOH

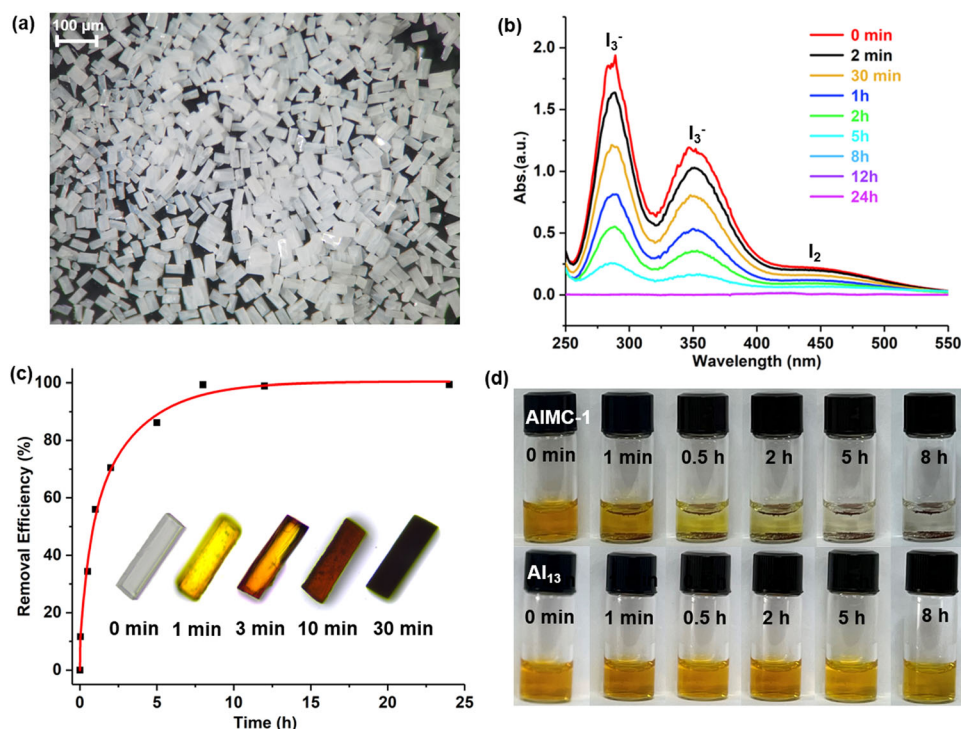


**Fig. 5 | Iodine removal by AIMC-1 crystals in 400 ppm I<sub>2</sub>/KI aqueous.** **a** Uniformly sized single-crystal adsorbents (~50 μm) ready for removing iodine from water. **b** Time-dependent UV-Vis spectra upon the addition of AIMC-1. **c** The iodine adsorption removal efficiency is based on the absorption peak at 286 nm. Inset: The

color change of single crystals during iodine adsorption (1 mL, 400 ppm). **d** the comparison of iodine adsorption between AIMC-1 and the Al<sub>13</sub> cluster reported in the literature<sup>23</sup>. Source data are provided as a Source Data file.

guests in AIMC-1 have been replaced by iodide ions after 30 min (Supplementary Fig. 116). The characteristic absorptions of I<sub>3</sub><sup>-</sup> and I<sub>2</sub> in the UV-vis spectra<sup>46</sup> in the aqueous solution of I<sub>2</sub>/KI decrease in intensity with time until equilibrium is reached after 8 h, with the iodine removal efficiency being up to 99% (Fig. 5c). Using the cationic Al<sub>13</sub> cluster ([AlO<sub>4</sub>Al<sub>12</sub>(μ<sub>2</sub>-OH)<sub>12</sub>(OCH<sub>2</sub>CH<sub>2</sub>OH)<sub>12</sub>]<sup>7+</sup>) with the same weight for comparison<sup>23</sup>, AIMC-1 exhibits a faster adsorption rate and a higher removal efficiency (Fig. 5d).

To explore the adsorption range further, we evaluated the iodine adsorption behavior of AIMC-1 by using I<sub>2</sub>/KI solutions with different concentrations (4, 40, 400, 2000 to 100,000 ppm). In all cases, the color of the crystals exhibited a noticeable change after 48 h adsorption, and the color is deeper at this point with higher concentration (Supplementary Figs. 117–123). The iodine-loaded crystalline samples were also characterized by EDS, X-ray photoelectron spectroscopy (XPS), Raman, and PXRD. The EDS and XPS results show increases in the amount of iodine absorbed with increased concentration of the I<sub>2</sub>/KI solutions used (Supplementary Figs. 124 and 125). As can be seen from the expanded XPS spectra (Fig. 6a), the two peaks for the I 3d transition move to the higher binding energy with increased iodine loading, indicating an enhanced degree of aggregation<sup>47,48</sup>. The intensities of the Raman signals also increase with the concentration of the I<sub>2</sub>/KI solution used (Fig. 6b). The band of 110 cm<sup>-1</sup> can be attributed to the symmetric stretching vibration of I<sub>3</sub><sup>-</sup><sup>49</sup>, the peak of 150 cm<sup>-1</sup> belongs to the asymmetric stretching vibration of I<sub>3</sub><sup>-</sup>, and the peak at 220 cm<sup>-1</sup> is attributed to the I-I stretching vibration. The latter is different from “free” I<sub>2</sub> dissolved in a nonpolar solvent (~211 cm<sup>-1</sup>)<sup>50</sup>, indicating that the confined I<sub>2</sub> molecules in AIMC-1 have strong interactions with the host. In addition, with increased iodine loading, new diffraction peaks in the PXRD can be observed, indicating that there is a significant host-guest interaction between iodine species and the host lattice (Fig. 6c)<sup>15</sup>.

In order to understand the capture process on a microscopic level, we carried out mechanistic studies using single-crystal X-ray diffraction on crystals obtained from the above iodine adsorption experiments at different iodine concentrations. The results from this detailed analysis provide ‘snapshots’ of the entry of iodine species into the host lattice and Al<sub>24</sub> unit as the concentration is increased and are shown in Fig. 6d. Porous AIMC-1 provides several sites for iodine incorporation, with the adsorption sites in the crystal lattice being gradually occupied with increased concentration from intermolecular to intramolecular. The iodine guests first enter the hydrophobic intermolecular channels (site 1, 4–400 ppm, C-H⋯I interactions: 2.317–4.067 Å and I⋯π interactions: 3.279–4.575 Å) and the intermolecular μ<sub>2</sub>-OH windows (site 2, 4 ppm, O-H⋯I: 2.887–3.196 Å) (Supplementary Figs. 126–129), then into the Al<sub>8</sub> macrocyclic units of the Al<sub>24</sub> units (site 3, 2000 ppm, C-H⋯I interactions: 2.820–3.387 Å and I⋯π interactions: 4.799–4.885 Å) (Supplementary Fig. 130), and finally occupying the interior cavity of the Al<sub>24</sub> units (site 4, 100,000 ppm, O-H⋯I interactions: 2.928–3.113 Å) (Supplementary Fig. 131). The exact nature of all of the iodine species present in the lattice at every stage cannot be deduced unambiguously from the X-ray data due to the disordering of the iodine sites. At 4 ppm I<sub>2</sub>/KI<sub>(aq)</sub>, the intermolecular channels can capture I<sub>3</sub><sup>-</sup> ions (Supplementary Fig. 126b), and the occupancy of these increases with concentration (40 ppm) (Supplementary Fig. 127a). Then iodine atoms continue to accumulate at site 1 until they reach saturation (Supplementary Fig. 128). Subsequently, I<sub>2</sub> molecules and disordered iodine species appear at site 3 (2000 ppm) (Supplementary Fig. 130e) and site 4 (100,000 ppm) (Supplementary Fig. 131e). It can be noted that the simulated PXRD patterns are consistent with experimental patterns for the iodine-loaded samples, indicating the evolution of the iodine species proposed analysis from SCXRD is rational (Supplementary Figs. 132–136).

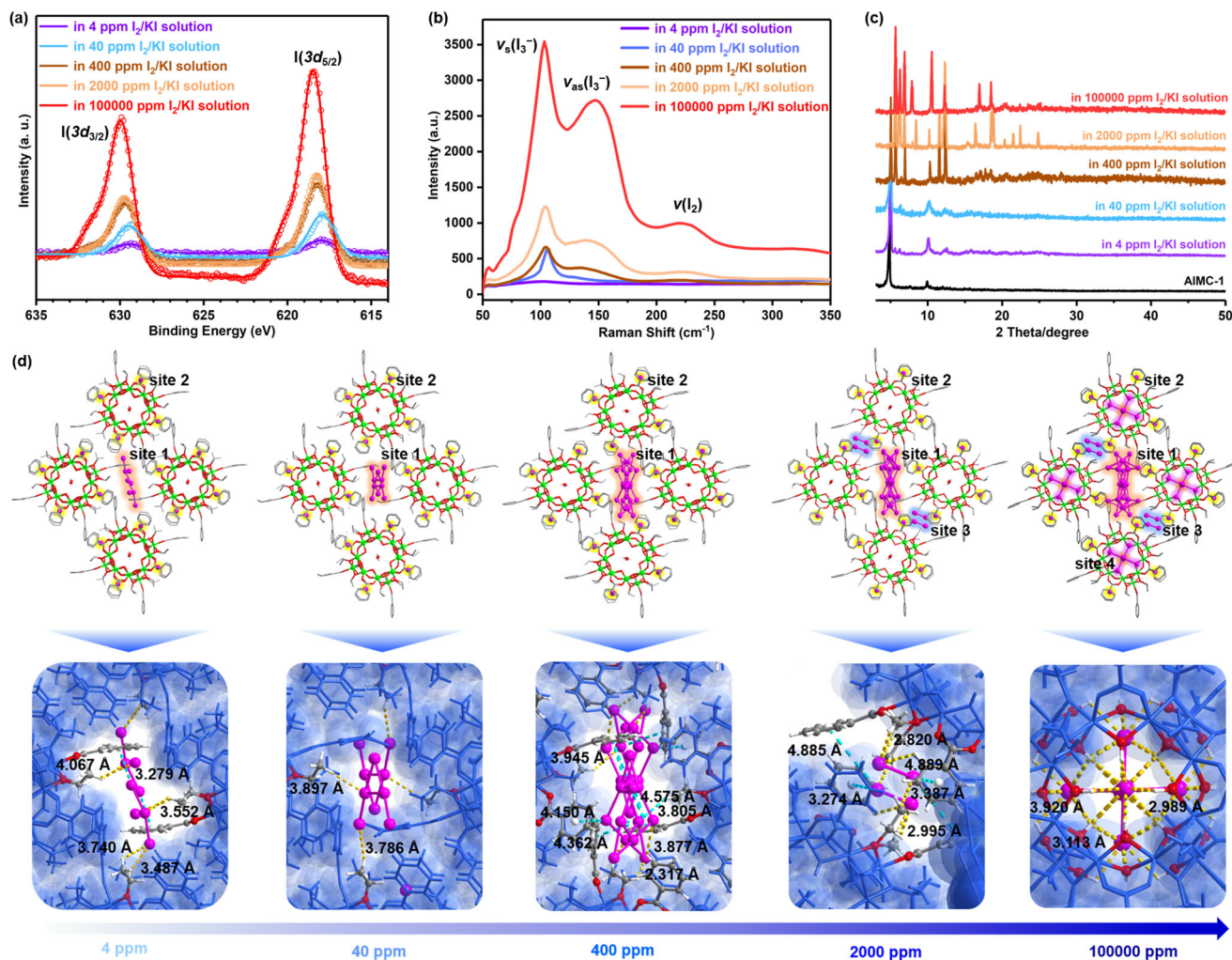


**Fig. 6 | Characterization and mechanism of the iodine capture processes of AIMC-1 in 4–100,000 ppm I<sub>2</sub>/KI aqueous solutions.** Macroscopic characterization of AIMC-1 after immersing in 4–100,000 ppm I<sub>2</sub>/KI aqueous solutions, including **a** expanded XPS spectra, **b** Raman spectra, and **c** PXRD patterns. **d** Mechanistic studies at the molecular level (top row: adsorption site; bottom row: corresponding supramolecular interactions between iodine species and Al<sub>24</sub> cage

hosts; site 1 intermolecular channel; site 2 square window of O<sub>24</sub>-*tro* cage; site 3 Al<sub>8</sub> macrocyclic cavity; site 4 the O<sub>8</sub> cavity of Al<sub>24</sub> cages). The strong hydrogen-bond interactions (C–H···I and O–H···I) are represented by yellow dotted bonds, while the I–π interactions are expressed by blue dotted bonds (Al: bright green; O: red; C: gray; H: white; N: blue; Cl: sea green; Br: purple; I: pink). Source data are provided as a Source Data file.

Such a low-concentration iodine/iodide capture ability suggests that AIMC compounds of the type described in this paper may be of value in the capture of environmental iodide/iodine (e.g., waste-water streams). We evaluated the adsorption capacity of AIMC-1 using a 100,000 ppm I<sub>2</sub>/KI aqueous solution based on the results of single-crystal analysis, which is about 820.3 mg/g. This value is slightly lower than that obtained from gravimetric (1.03 g/g) and titrimetric analysis (890 mg I<sub>2</sub>/g)<sup>13,15,51</sup>, which may be due to the disorder of the iodine species in the lattice and difficulty in determining the precise composition by X-ray single-crystal analysis. Even so, the capacity of AIMC-1 is still higher than that of MOFs (Supplementary Table 9)<sup>52,53</sup> and noble metal-based adsorbents<sup>54–56</sup>. The iodine-loaded crystals of AIMC-1 can be reused as iodine sponges after the removal of the iodine components by washing them with HOEt (Supplementary Fig. 137). PXRDs of AIMC-1 after 200 kGy β or γ irradiation also indicate no structural degradation (Supplementary Fig. 138a), and the retention of the adsorption capacity compared to non-irradiated samples (Supplementary Fig. 138b). This is important in regard to the potential applications of these adsorbents in the removal of radioactive iodine.

In this paper, we explored the structural landscape of a series of unique solid-state materials based on a cationic Al<sub>24</sub> Archimedean

host. The highly symmetrical Al<sub>24</sub> cage has a purely inorganic *tcu* kernel and six calixarene-like Al<sub>8</sub> shells. The core–shell arrangement is highly adaptive toward a variety of guests (NO<sub>3</sub><sup>−</sup>, OEt<sup>−</sup>, O<sup>−</sup>Pr<sup>−</sup>, Cl<sup>−</sup>, Br<sup>−</sup>, and I<sup>−</sup>), generating a broad range of supramolecular lattice arrangements in the solid-state. The unique structural features (simultaneously containing hydrophobic outer channels and a hydrophilic inner cavity) make these materials highly stable in water. Iodine/iodide capture experiments have revealed rapid enrichment, low-concentration capture, high adsorption capacity, recyclability, and radiation-resistant characteristics for AIMC-1, indicating its potential applications in trace iodine extraction in waste-water streams (such as in the radiation industry). These host assemblies provide alternatives to organic hosts such as calixarenes, crown ethers, and pillararenes, for water purification.

## Methods

### Syntheses of AIMC compounds

AIMC-1 to AIMC-7 were synthesized by mixed Al(O<sup>−</sup>Pr)<sub>3</sub> (6 mmol), benzoic acid (3 mmol), HNO<sub>3</sub> (60–100 μL) in 8–10 mL alcohols solvent (HOEt or HO<sup>−</sup>Pr). The trace of HNO<sub>3</sub> plays an important role in the formation of the Al<sub>24</sub> cages. Its use should be controlled between 60

and 100  $\mu\text{L}$  in this reaction. Besides, the addition of extra guests greatly affects the supramolecular assembly of  $\text{Al}_{24}$  cages, such as  $\text{H}_2\text{O}$ , benzyl alcohol, quaternary ammonium salt and pyrazole. Notably, water helps to increase the yield, for example, it increased from -11% to -43% when 60  $\mu\text{L}$   $\text{H}_2\text{O}$  is introduced in the reaction system of **AIMC-1**. See Supplementary Methods for more details on the synthesis of all of the compounds described in this paper.

### Scale-up synthesis of AIMC-1

A mixture of  $\text{Al}(\text{O}^i\text{Pr})_3$  (6.0 g), benzoic acid (1.8 g),  $\text{HNO}_3$  (0.5 mL),  $\text{H}_2\text{O}$  (300  $\mu\text{L}$ ), and ethanol (40 mL) was sealed in an 80 mL vial and heat at 80  $^\circ\text{C}$  for 7 days. When cooled to room temperature, the white precipitate and colorless crystals are washed by ethanol repeatedly. After drying, the precipitate and crystals are passed through a 200-mesh sieve, and pure-phase rectangular crystals are obtained. (Yield: -817 mg, -16% based on  $\text{Al}(\text{O}^i\text{Pr})_3$ ).

### Iodine adsorption

Crystals with moderate size were selected for iodine adsorption research. Large crystals tend to fracture during adsorption, while the X-ray diffraction intensity for tiny-size crystals is very weak. Thus, we choose -15  $\mu\text{m}$   $\times$  50  $\mu\text{m}$  crystals for iodine adsorption measurements. A 20 mg sample was immersed in  $\text{I}_2/\text{KI}$  aqueous (10 mL) with various concentrations for 48 h at room temperature. The iodine-loaded samples obtained were filtered and washed prior to characterizations (XPS, EDS, Raman, and PXRD) and SCXRD. To measure the adsorption capacity, **AIMC-1** crystalline samples (50 mg) were soaked in 100,000 ppm  $\text{I}_2/\text{KI}_{(\text{aq})}$  (300 mg KI and 300 mg  $\text{I}_2$  in 3 mL  $\text{H}_2\text{O}$ ) for 48 h. The iodine-saturated samples were collected by filtration, washing with water (2 mL  $\times$  30 times) until the filtrate became clear, and dried in air for gravimetric analysis and characterization. The filtrate was collected and 2 mL 2% aqueous starch indicator was added for sodium bisulfite titration analysis.

### Regeneration and recycling experiment

Iodine-loaded samples were immersed in HOEt (2 mL) for desorption of the iodine/iodide, during which the solvent was decanted and washing repeatedly several times. The desorption was observed to take place rapidly. Once HOEt is added, the color of the solution turned yellow immediately and then gradually deepened. This process can be investigated using time-dependent UV-Vis spectra.

### Irradiation stability measurements

**AIMC-1** (100 mg) was irradiated at a dose rate of 20 kGy/h for 10 h using a  $^{60}\text{Co}$   $\beta$ - or  $\gamma$ -irradiation source.  $\beta$ -Irradiation was provided by an electron accelerator located at the CGD Dasheng Electron Accelerator Co., Ltd., in Jiangsu Province, China. While  $\gamma$ -irradiation was conducted by Gansu Tianchen Irradiation Technology Co., Ltd., in Gansu Province, China.

**Caution.**  $\text{HNO}_3$  is corrosive and has a pungent odor. Thus, the experiments should be carried out in a fume hood, and gloves and masks should be worn.

### Data availability

X-ray crystallographic data for the structures reported in the article have been deposited at the Cambridge Crystallographic Data Centre, under deposition numbers CCDC 2193096 (**AIOC-60**), 2193097 (**AIMC-1**), 2193098 (**AIMC-2**), 2193099 (**AIMC-3**), 2193100 (**AIMC-4**), 2193101 (**AIMC-5**), 2193102 (**AIMC-6**), 2193103 (**AIMC-7**), 2193104 (**AIMC-8**), 2193105 (**AIMC-1a**), 2193106 (**I@Al<sub>24</sub>-400 ppm-30 min**), 2193107 (**I@Al<sub>24</sub>-400 ppm-48 h**), 2193108 (**I@Al<sub>24</sub>-40 ppm-48 h**), 2193109 (**I@Al<sub>24</sub>-400 ppm-48 h**), 2193110 (**I@Al<sub>24</sub>-2000 ppm-48 h**) and 2193111 (**I@Al<sub>24</sub>-100,000 ppm-48 h**). Copies of the data can be obtained free of charge via <https://www.ccdc.cam.ac.uk/structures/>.

The dataset is also provided as Supplementary Data 1 with this paper. All other data supporting the findings of this study are available within the paper, its supplementary information, or the corresponding author. Source data are provided with this paper.

### References

- Sava, D. F. et al. Capture of volatile iodine, a gaseous fission product, by zeolitic imidazolate framework-8. *J. Am. Chem. Soc.* **133**, 12398–12401 (2011).
- Watanabe, Y. et al. Novel long-term immobilization method for radioactive iodine-129 using a zeolite/apatite composite sintered body. *ACS Appl. Mater. Interfaces* **1**, 1579–1584 (2009).
- Küpper, F. C. et al. Commemorating two centuries of iodine research: an interdisciplinary overview of current research. *Angew. Chem. Int. Ed.* **50**, 11598–11620 (2011).
- Yu, X., Cui, W., Zhang, F., Guo, Y. & Deng, T. Removal of iodine from the salt water used for caustic soda production by ion-exchange resin adsorption. *Desalination* **458**, 76–83 (2019).
- Chapman, K. W., Chupas, P. J. & Nenoff, T. M. Radioactive iodine capture in silver-containing mordenites through nanoscale silver iodide formation. *J. Am. Chem. Soc.* **132**, 8897–8899 (2010).
- Liu, L. et al. Selective capture of iodide from solutions by microrosette-like  $\delta\text{-Bi}_2\text{O}_3$ . *ACS Appl. Mater. Interfaces* **6**, 16082–16090 (2014).
- Zhang, T. et al. Hierarchically porous bismuth oxide/layered double hydroxide composites: preparation, characterization and iodine adsorption. *J. Clean. Prod.* **144**, 220–227 (2017).
- Liu, J., Huang, J., Niu, W., Tan, C. & Zhang, H. Unconventional-phase crystalline materials constructed from multiscale building blocks. *Chem. Rev.* **121**, 5830–5888 (2021).
- Sheng, D. et al. Efficient and selective uptake of  $\text{TcO}_4^-$  by a cationic metal-organic framework material with open  $\text{Ag}^+$  sites. *Environ. Sci. Technol.* **51**, 3471–3479 (2017).
- Zhu, L. et al. Identifying the recognition site for selective trapping of  $^{99}\text{TcO}_4^-$  in a hydrolytically stable and radiation resistant cationic metal-organic framework. *J. Am. Chem. Soc.* **139**, 14873–14876 (2017).
- Lin, Q.-F. et al. A stable aluminosilicate zeolite with intersecting three-dimensional extra-large pores. *Science* **374**, 1605–1608 (2021).
- Zheng, N., Bu, X., Wang, B. & Feng, P. Microporous and photoluminescent chalcogenide zeolite analogs. *Science* **298**, 2366–2369 (2002).
- Gogia, A., Das, P. & Mandal, S. K. Tunable strategies involving flexibility and angularity of dual linkers for a 3D metal-organic framework capable of multimedia iodine capture. *ACS Appl. Mater. Interfaces* **12**, 46107–46118 (2020).
- Liu, Q.-K., Ma, J.-P. & Dong, Y.-B. Highly efficient iodine species enriching and guest-driven tunable luminescent properties based on a cadmium(II)-triazole MOF. *Chem. Commun.* **47**, 7185–7187 (2011).
- Lin, Y. et al. An elastic hydrogen-bonded cross-linked organic framework for effective iodine capture in water. *J. Am. Chem. Soc.* **139**, 7172–7175 (2017).
- Hua, B., Shao, L., Li, M., Liang, H. & Huang, F. Macrocyclic-based solid-state supramolecular polymers. *Acc. Chem. Res.* **55**, 1025–1034 (2022).
- Jie, K., Zhou, Y., Li, E. & Huang, F. Nonporous adaptive crystals of pillarenes. *Acc. Chem. Res.* **51**, 2064–2072 (2018).
- Hasell, T., Schmidtman, M. & Cooper, A. I. Molecular doping of porous organic cages. *J. Am. Chem. Soc.* **133**, 14920–14923 (2011).
- Su, C.-Y., Yang, X.-P., Kang, B.-S. & Mak, T. C. W.  $T_h$ -symmetric nanoporous network built of hexameric metallamacrocycles with disparate. *Angew. Chem. Int. Ed.* **40**, 1725–1728 (2001).



20. Luo, D., He, Y., Tian, J., Sessler, J. L. & Chi, X. Reversible iodine capture by nonporous adaptive crystals of a bipyridine cage. *J. Am. Chem. Soc.* **144**, 113–117 (2022).
21. Zheng, S.-T., Zhang, J., Li, X.-X., Fang, W.-H. & Yang, G.-Y. Cubic polyoxometalate-organic molecular cage. *J. Am. Chem. Soc.* **132**, 15102–15103 (2010).
22. Dolbecq, A., Dumas, E., Mayer, C. R. & Mialane, P. Hybrid organic–inorganic polyoxometalate compounds: from structural diversity to applications. *Chem. Rev.* **110**, 6009–6048 (2010).
23. Gu, B. et al. Synthesis, characterization and properties of a glycol-coordinated epsilon-Keggin-type  $Al_{13}$  chloride. *Chem. Commun.* **54**, 4148–4151 (2018).
24. Abeyasinghe, S., Unruh, D. K. & Forbes, T. Z. Crystallization of Keggin-type polyaluminum species by supramolecular interactions with disulfonate anions. *Cryst. Growth Des.* **12**, 2044–2051 (2012).
25. Jin, X. et al. Insight into the structural characteristics of core-links and flat-aluminum tridecamers: a density functional theory study. *Dalton Trans.* **41**, 1027–1032 (2012).
26. Geng, L., Liu, C. H., Wang, S. T., Fang, W. H. & Zhang, J. Designable aluminum molecular rings: ring expansion and ligand functionalization. *Angew. Chem. Int. Ed.* **59**, 16735–16740 (2020).
27. Liu, C. H. et al. Designable assembly of aluminum molecular rings for sequential confinement of iodine molecules. *Angew. Chem. Int. Ed.* **60**, 21426–21433 (2021).
28. Yao, S., Fang, W. H., Sun, Y., Wang, S. T. & Zhang, J. Mesoporous assembly of aluminum molecular rings for iodine capture. *J. Am. Chem. Soc.* **143**, 2325–2330 (2021).
29. Li, Y. et al. Record aluminum molecular rings for optical limiting and nonlinear optics. *Angew. Chem. Int. Ed.* **61**, e202116563 (2022).
30. Spandl, J., Brüdgam, I. & Hartl, H. Solvothermal synthesis of a 24-nuclear, cube-shaped squarato-oxovanadium(IV) framework:  $[N(nBu)_4]_8[V_{24}O_{24}(C_4O_4(OCH_3)_{12})_{32}]$ . *Angew. Chem. Int. Ed.* **40**, 4018–4020 (2001).
31. Domoto, Y., Abe, M. & Fujita, M. A highly entangled  $(M_3L_2)_8$  truncated cube from the anion-controlled oligomerization of a  $\pi$ -coordinated  $M_3L_2$  subunit. *J. Am. Chem. Soc.* **143**, 8578–8582 (2021).
32. Su, K., Wang, W., Du, S., Ji, C. & Yuan, D. Efficient ethylene purification by a robust ethane-trapping porous organic cage. *Nat. Commun.* **12**, 3703 (2021).
33. Goeb, S. & Salle, M. Electron-rich coordination receptors based on tetrathiafulvalene derivatives: controlling the host–guest binding. *Acc. Chem. Res.* **54**, 1043–1055 (2021).
34. Tang, X. et al. Endohedral functionalization of chiral metal-organic cages for encapsulating achiral dyes to induce circularly polarized luminescence. *Chem* **7**, 2771–2786 (2021).
35. Ratajczak, H. & Orville-Thomas, W. J. Hydrogen-bond studies. Part I. The relation between vibrational frequencies and bond length in O–H...H hydrogen-bonded systems. *J. Mol. Struct.* **68**, 449–461 (1967).
36. Zhao, M. M. & Shi, P. P. Melaminium iodide monohydrate. *Acta Crystallogr.* **E66**, o1415 (2010).
37. Pavel, I., Cervantes-Lee, F., Haiduc, I. & Pannell, K. H. Supramolecular self-assembly involving cooperative use of dative coordinate, secondary and hydrogen bonding in solid  $[(Me_3Sn)_3(\mu-OH)_2]+Br^-$ . *Inorg. Chem. Commun.* **4**, 530–533 (2001).
38. Harmon, K. M., Toccalino, P. L. & Janos, M. S. Hydrogen Bonding Part 29. Thermodynamics of dissociation and stoichiometric study of the lower hydrates of tetraethylammonium and tetrapropylammonium chlorides. *J. Mol. Struct.* **213**, 193–200 (1989).
39. Deng, Y. K. et al. Hierarchical assembly of a  $\{Mn^{II}_5Mn^{III}_4\}$  Brucite disc: step-by-step formation and ferrimagnetism. *J. Am. Chem. Soc.* **138**, 1328–1334 (2016).
40. Guo, L. Y. et al. Core-shell  $\{Mn_7C(Mn,Cd)_{12}\}$  assembled from core  $\{Mn_7\}$  disc. *J. Am. Chem. Soc.* **139**, 14033–14036 (2017).
41. Wang, C., Liu, X., Keser Demir, N., Chen, J. P. & Li, K. Applications of water stable metal-organic frameworks. *Chem. Soc. Rev.* **45**, 5107–5134 (2016).
42. Low, J. J. et al. Virtual high throughput screening confirmed experimentally: porous coordination polymer hydration. *J. Am. Chem. Soc.* **131**, 15834–15842 (2009).
43. Cychosz, K. A. & Matzger, A. J. Water stability of microporous coordination polymers and the adsorption of pharmaceuticals from water. *Langmuir* **26**, 17198–17202 (2010).
44. Bai, Y. et al. Zr-based metal-organic frameworks: design, synthesis, structure, and applications. *Chem. Soc. Rev.* **45**, 2327–2367 (2016).
45. Huang, M., Yang, L., Li, X. & Chang, G. An indole-derived porous organic polymer for the efficient visual colorimetric capture of iodine in aqueous media via the synergistic effects of cation- $\pi$  and electrostatic forces. *Chem. Commun.* **56**, 1401–1404 (2020).
46. Pursell, J. L. & Pursell, C. J. Host–guest inclusion complexation of  $\alpha$ -cyclodextrin and triiodide examined using UV–Vis spectrophotometry. *J. Phys. Chem. A* **120**, 2144–2149 (2016).
47. Xie, Y. et al. Ionic functionalization of multivariate covalent organic frameworks to achieve an exceptionally high iodine-capture capacity. *Angew. Chem. Int. Ed.* **60**, 22432–22440 (2021).
48. Tang, Y., Huang, H., Li, J., Xue, W. & Zhong, C. IL-induced formation of dynamic complex iodide anions in IL@MOF composites for efficient iodine capture. *J. Mater. Chem. A* **7**, 18324–18329 (2019).
49. Wang, J. et al. Hydrogen bond-mediated strong adsorbent- $I_3^-$  interactions enable high-efficiency radioiodine capture. *Mater. Horiz.* **6**, 1517–1525 (2019).
50. Banerjee, D. et al. Iodine adsorption in metal-organic frameworks in the presence of humidity. *ACS Appl. Mater. Interfaces* **10**, 10622–10626 (2018).
51. Xie, L. et al. Calix[4]pyrrole-based crosslinked polymer networks for highly effective iodine adsorption from water. *Angew. Chem. Int. Ed.* **61**, e202113724 (2022).
52. Long, X. et al. Removal of iodine from aqueous solution by PVDF/ZIF-8 nanocomposite membranes. *Sep. Purif. Technol.* **238**, 116488 (2020).
53. Xu, L. et al. A pillared double-wall metal-organic framework adsorption membrane for the efficient removal of iodine from solution. *Sep. Purif. Technol.* **274**, 118436 (2021).
54. Bo, A. et al. Removal of radioactive iodine from water using  $Ag_2O$  grafted titanate nanolamina as efficient adsorbent. *J. Hazard. Mater.* **246–247**, 199–205 (2013).
55. Xiong, Y. et al. Cellulose fibers constructed convenient recyclable 3D graphene-formicary-like  $\delta$ - $Bi_2O_3$  aerogels for the selective capture of iodide. *ACS Appl. Mater. Interfaces* **9**, 20554–20560 (2017).
56. Yang, D. et al. Capture of radioactive cesium and iodide ions from water by using titanate nanofibers and nanotubes. *Angew. Chem. Int. Ed.* **50**, 10594–10598 (2011).

## Acknowledgements

This work is supported by the National Natural Science Foundation of China (92061104, 21935010), Natural Science Foundation of Fujian Province (2021J06035), and Youth Innovation Promotion Association CAS (2017345 and Y2021081).

## Author contributions

W.-H.F. and J.Z. conceived and designed this project. Y.-J.L. carried out the synthesis, characterization, and iodine adsorption study. Y.-F.S. assisted with sample characterization and data analysis. S.-H.S. and Z.-H.L. gave support on the scale-up synthesis. S.-T.W. assisted with structural determination. W.-H.F., J.Z., D.S.W., and Y.-J.L. wrote the manuscript. All the authors discussed the results and commented on the manuscript.

## Competing interests

The authors declare no competing interests.

## Additional information

**Supplementary information** The online version contains supplementary material available at <https://doi.org/10.1038/s41467-022-34296-4>.

**Correspondence** and requests for materials should be addressed to Wei-Hui Fang or Jian Zhang.

**Peer review information** *Nature Communications* thanks Xiaodong Chi, Baiyan Li and the other, anonymous, reviewer(s) for their contribution to the peer review of this work. Peer reviewer reports are available.

**Reprints and permissions information** is available at <http://www.nature.com/reprints>

**Publisher's note** Springer Nature remains neutral with regard to jurisdictional claims in published maps and institutional affiliations.

**Open Access** This article is licensed under a Creative Commons Attribution 4.0 International License, which permits use, sharing, adaptation, distribution and reproduction in any medium or format, as long as you give appropriate credit to the original author(s) and the source, provide a link to the Creative Commons license, and indicate if changes were made. The images or other third party material in this article are included in the article's Creative Commons license, unless indicated otherwise in a credit line to the material. If material is not included in the article's Creative Commons license and your intended use is not permitted by statutory regulation or exceeds the permitted use, you will need to obtain permission directly from the copyright holder. To view a copy of this license, visit <http://creativecommons.org/licenses/by/4.0/>.

© The Author(s) 2022